Obtaining reliable source locations with Time Reverse Imaging: limits to array design, velocity models and signal-to-noise ratios

Claudia Werner[1,2] and Erik H. Saenger[1,2]

[1]International Geothermal Center Bochum, Lennershofstr. 140, 44801 Bochum, Germany
[2]Ruhr-University Bochum, Universitätsstr. 150, 44801 Bochum, Germany

Correspondence: Claudia Werner (claudia.werner@hs-bochum.de)

Abstract. Time Reverse Imaging (TRI) is evolving into a standard technique for locating and characterizing seismic events. In recent years, TRI has been applied to a wide range of applications from the lab scale over the field scale up to the global scale. No identification of events and their onset times is necessary when locating events with TRI. Therefore, it is especially suited for locating quasi-simultaneous events and events with a low signal-to-noise ratio. However, in contrast to more regularly
5   applied localization methods, the prerequisites for applying TRI are not sufficiently known.

To investigate the significance of station distributions, complex velocity models and signal-to-noise ratios for the location accuracy, numerous simulations were performed using a finite difference code to propagate elastic waves through three-dimensional models. Synthetic seismograms were reversed in time and re-inserted into the model. The time-reversed wavefield backpropagates through the model and, in theory, focuses at the source location. This focusing was visualized using imaging
10   conditions. Additionally, artificial focusing spots were removed with an illumination map specific to the setup. Successful locations were sorted into four categories depending on their reliability. Consequently, individual simulation setups could be evaluated by their ability to produce reliable source locations.

Optimal inter-station distances, minimum apertures, relations between array and source location, heterogeneities of inter-station distances and total number of stations were investigated for different source depth as well as source types. Additionally,
15   the accuracy of the locations was analysed when using a complex velocity model or a low signal-to-noise ratio.

Finally, an array in Southern California was investigated for its ability to locate seismic events in specific target depths while using the actual velocity model for that region. In addition, the success rate with recorded data was estimated.

Knowledge about the prerequisites for using TRI enables the estimation of success rates for a given problem. Furthermore, it reduces the time needed for adjusting stations to achieve more reliable locations and provides a foundation for designing
20   arrays for applying TRI.

1   Introduction

The localization and characterization of seismic events in the subsurface is crucial for understanding physical processes in the Earth. Well-established methods are able to locate most seismic events in a fast and reliable manner; but they rely on identifiable onsets of events. Time Reverse Imaging (TRI) is a method especially suited for locating and characterizing events

which are indistinguishable in traces because they occur quasi-simultaneously or are superposed by noise. The prerequisites for more regularly applied localization methods are very well known. However, which station distributions, which degree of complexity in the velocity model and which level of noise hinder or enhance locating events with TRI is not sufficiently known. Therefore, this study systematically tests different station distributions for their localization capabilities while considering complex velocity models and low signal-to-noise ratios.

TRI uses the whole recorded waveform rendering the identification of events and their onsets obsolete. It can be applied as long as the wave propagation can be described with a time-invariant wave equation. Seismic traces are reversed in time and backpropagated through a medium until they focus on the initial event location. Imaging conditions are used to visualize aspects of the backpropagating wavefield and obtain the source location.

TRI has been applied in earth sciences as well as medical sciences for some time (Fink et al., 1999). In recent years multiple studies have shown that TRI is an easy-to-use and reliable localization tool: It has been used to retrieve source information on various scales from the lab scale in non-destructive testing (Saenger, 2011; Anderson et al., 2011; Harker and Anderson, 2013; Kocur et al., 2016) over the field scale, for example in volcanic tremor (Lokmer et al., 2009) and non-volcanic tremor applications (Larmat et al., 2009; Horstmann et al., 2015) and above hydrocarbon reservoirs (Steiner et al., 2008), up to the global scale (Larmat et al., 2006, 2008). However, to apply TRI, a fairly accurate velocity model is needed to accurately backpropagate the wavefield. With increasing availability of high resolution large three-dimensional velocity models and the knowledge about prerequisites, TRI has the potential to locate seismic events, which could not be located reliably thus far, in a wide range of applications.

1.1 Restrictions to the localization capabilities of TRI

The estimation of location accuracy is one major challenge when applying TRI. A common approach is, therefore, to perform a preliminary synthetic study to test if the given velocity model and station distribution enable reliable locations. If the synthetic study fails, the setup is adjusted until either the study is abandoned or a sufficiently reliable result is achieved. This adjustment phase can be time-consuming because there are multiple characteristics appearing at once that may hinder the localization.

Numerous characteristics of where stations are placed at the surface seem to influence the chance of success with TRI significantly. In theory, TRI works with only one station (Montagner et al., 2012). Nevertheless, in most cases more stations are needed to obtain a stable result. Therefore, the total number of stations is often considered to have a major influence on the success or failure of obtaining accurate source locations (Kremers et al., 2011; Horstmann et al., 2015). However, numerous reports state that a smaller amount of stations works just as well (Gajewski and Tessmer, 2005; Steiner et al., 2008; Lokmer et al., 2009; Larmat et al., 2009).

The aperture of the array seems to be another characteristic of the station distribution influencing location accuracy. Steiner et al. (2008) and Lokmer et al. (2009) report false locations in the two-dimensional case when the aperture of the array is limited. Artman et al. (2010) emphasize the importance of a sufficiently large aperture to obtain a spatially focused location.

Distances between the individual stations and the homogeneity of these inter-station distances seem to be important as well (Lokmer et al., 2009). Furthermore, the azimuthal gap, which is the angle between two stations viewed from the epicentre

2

location, is introduced by Horstmann et al. (2015). It is an indirect measurement for the heterogeneity of inter-station distances. Horstmann et al. (2015) observe an enhanced localization result if the maximum azimuthal gap is small. Lokmer et al. (2009) and Horstmann et al. (2015) also note a different quality of focusing for sources in different depths while using the same stations.

5 In addition to the placement of stations, the velocity model can significantly influence the success rate of TRI. A velocity model that differs from the true velocity model may inhibit the localization of real events. However, if the error is small enough, TRI is still successful (Gajewski and Tessmer, 2005; Lokmer et al., 2009; Saenger, 2011). Similarly, a smoothed velocity model does not significantly influence the results (Gajewski and Tessmer, 2005). Furthermore, complex velocity structures like low-velocity zones or sharp velocity contrasts may inhibit the application of TRI even when using synthetic data (Larmat et al.,
10 2009). Nevertheless, necessary simplifications due to the availability of velocity models may inhibit localization of real events with TRI (Artman et al., 2010; Horstmann et al., 2015). Common simplifications include the usage of a constant ratio of p-wave velocity to s-wave velocity or a constant density.

 A high level of noise in the traces may inhibit the localization with TRI, even when the array and the velocity model are sufficiently good. In theory, TRI works even with a very low signal-to-noise ratio because noise is random and will not
15 superpose constructively to form a focus during the backpropagation of the wavefield. Gajewski and Tessmer (2005) show traces with events not distinguishable from the noise and TRI is still able to reconstruct the source location. Witten and Artman (2011) create synthetic data with signal-to-noise ratios as low as 0.25 and show successful locations. Nevertheless, they observe a decrease in location accuracy with lower signal-to-noise ratios.

1.2 Objective of this study

20 This study aims at finding station distributions producing reliable source locations with TRI. Finding these optimal station distributions is crucial to estimate the success rate of TRI with a given set of stations. Additionally, the time needed to adjust station distributions may be decreased. Furthermore, the prerequisites of the method should be known when designing an array for using TRI. Therefore, the influence of the station distribution, the complexity of the velocity model and the rate of noise on the location accuracy were investigated.

25 We performed numerous simulations to systematically analyse different station distributions and their influence on the location accuracy of sources in different depths as well as of different source types. The focus was thereby on the distance between receivers, the symmetry of the array in relation to the source position, the azimuthal gap between receivers and the number of stations. Simulations were performed first with a homogeneous velocity model and afterwards with a complex velocity model. Location accuracy was investigated while the velocity model is known and when it is not known correctly. We
30 investigated the ability of TRI to cope with very low signal-to-noise ratios. To complete the study, we applied the guidelines found with the methodical tests to an actual example in Southern California. The ability to locate events in a target depth was investigated while using the existing array as well as the actual velocity model for that region by Zeng et al. (2016).

 With the example in Southern California we demonstrate how to assess the success rate of the localization with TRI using a synthetic study. Additionally, the station distribution was altered to enhance location accuracy. We give estimates in which part

of the model reliable locations can be expected. Additionally, we demonstrate how to design an array, which produces reliable source locations.

All simulations were performed using a finite difference scheme to propagate elastic waves through three-dimensional models. The advantage of a purely synthetic study is that the source location is known and subsequently the location accuracy can be estimated. Additionally, parameters influencing the localization could be tested individually.

2 The method of Time Reverse Imaging (TRI)

Time Reverse Imaging (TRI) uses the whole waveform of recorded seismograms to locate and characterize seismic events. The method consists of three steps following the workflow introduced by Saenger (2011) and modified by Witten and Artman (2011): Reversal of individual traces in time, backpropagation of time-reversed wavefield and elimination of artefacts impinged by velocity structure and model setup. Results are afterwards visualized using suitable imaging conditions. In the following, the adaptation of this workflow to this study is described in detail.

The method of TRI was investigated using synthetic seismograms created by forward simulations of the propagation of elastic waves through a suitable medium. In this study first a homogeneous medium and later a heterogeneous velocity model for Southern California was used. The obtained seismograms were not altered besides flipping them in time. Montagner et al. (2012) use binarized seismograms to demonstrate that TRI is based on the coherency of the phases in the seismograms and not on the amplitudes. Therefore, the phase information in the recorded seismograms should be kept as close to the original as possible and any filter should be a zero-phase filter to prevent phase shifts in the time domain. Additionally, all traces need to be time-synchronous.

The time-reversed seismograms were reinserted into the model domain at the exact locations they were recorded at. The receivers of the forward simulation act as sources in the time-reversed simulation. In this study, receivers always mean stations at the surface which act as receivers in forward simulations and sources in reverse simulations. The time-reversed wavefield backpropagates through the model and collapses at the initial source location.

Imaging conditions highlight specific characteristics of the backpropagating wavefield. They were used to visualize the point in space and time where the wavefield focuses. In this numerical study, the event time was known and the position of foci are compared to the source position used in the forward simulation to determine the accuracy of the event locations.

Apart from the focus spot at the initial source location, parts of the velocity structure and the model domain itself may be highlighted by artificial focusing spots. Usually, artificial focusing spots appear around the receiver positions at the surface of the model. Additionally, special velocity structures, like low velocity zones, may cause artificial focusing (Larmat et al., 2009). To eliminate those artefacts, the workflow introduced by Witten and Artman (2011) was used. Images produced with the specific imaging conditions were divided by images produced by the backpropagation of random noise. To keep amplitudes and frequency content the same, recorded seismograms were backpropagated through the model not time-reversed. The not time-reversed wavefield cannot focus on the initial source location and acts as a noise field. The result is an illumination map of the model highlighting areas where focusing occurs solely due to the used velocity structure and the model setup as described

by Witten and Artman (2011) . When dividing the results by this illumination map ideally only focusing spots created by interferences of the time-reversed traces remain in the image.

2.1 Simulation of Wave Propagation in Elastic Media

The wave propagation in three-dimensional elastic media for the forward as well as the backward simulation was performed using a finite difference code developed by Saenger et al. (2000). A second-order finite-difference operator was used in space as well as in time. The explicit finite difference operators for the used rotated staggered grid are discussed in Saenger et al. (2000). The model boundaries at the bottom and at the sides of the models were absorbing boundaries after Clayton and Engquist (1980) and the top boundary was a free surface that is incorporated as a vacuum layer.

A non-volcanic tremor application in Southern California was used as a real-life example. Therefore, the models used in this study were set up to be numerically stable when using the receivers used in Horstmann et al. (2015) and the updated velocity model by Zeng et al. (2016) that covers the same region as in Horstmann et al. (2015). All models span from $-65\,\mathrm{km}$ to $+65\,\mathrm{km}$ in x-direction, from $-70\,\mathrm{km}$ to $+50\,\mathrm{km}$ in y-direction and from the surface at $0\,\mathrm{km}$ to a depth of $28\,\mathrm{km}$. The grid spacing was set to $0.1\,\mathrm{km}$ to balance accuracy and stability in the simulations, while the time step was set to $0.01\,\mathrm{s}$. For the synthetic tests, a homogeneous velocity model with the same dimensions as the velocity model from Southern California was created.

Sources in the forward simulations were implemented as moment tensor sources. An explosion source (only $M_{xx} = M_{yy} = M_{zz}$ were non-zero and all were equal in strength) or a strike-slip source (only $M_{xy} = M_{yx}$ was non-zero) was used. As a source signal, the negative normalized second derivative of the Gaussian function, also called a Ricker wavelet, was used. The Ricker wavelet was implemented, following Shearer (2009), as

$$R(t) = (1 - 2\pi^2 f_p^2 t^2) \cdot exp(-\pi^2 f_p^2 t^2), \tag{1}$$

where t denotes the time and f_p the peak frequency of the wavelet. For all simulations in this study the peak frequency was set to $f_p = 1.75\,\mathrm{Hz}$ which results in a maximum frequency of about $f_{max} = 5\,\mathrm{Hz}$. In this frequency range non-volcanic tremor is usually observed (Horstmann et al., 2015). The wavelet was centred at $t = 0\,\mathrm{s}$.

The source position was set to $x = -1.8\,\mathrm{km}$ and $y = -28.3\,\mathrm{km}$, which corresponds to an existing recorded earthquake that was chosen randomly and represents one possible source location. The earthquake occurred at the 28th of June 2011 at 14:10 and had a magnitude of 1.68 (NCEDC, 2014). The three depths used for the sources are: $z_1 = 5\,\mathrm{km}, z_2 = 11.9\,\mathrm{km}$ and $z_3 = 22\,\mathrm{km}$. The deepest source represents the depth where non-volcanic tremor occurs. The medium depth is the depth of the example earthquake while the shallow source represents a shallow end-member and is not geologically relevant in the considered region in Southern California.

2.2 Imaging Conditions

Imaging conditions were used to visualize specific characteristics of the backpropagated wavefield. They were calculated as the maximum value of specific characteristics of the wavefield at each point x of the model domain over the whole simulation

time, from $t = 0$ s to $t = T$. A perfect result would be a single gridpoint with the highest value of the specific imaging condition at the initial source location and very low values everywhere else.

Numerous imaging conditions have been proposed in the past. Here we summarise characteristics of the wavefield that can be used to calculate imaging conditions. The most intuitive imaging condition uses the maximum amplitude of displacement (e.g. used in Gajewski and Tessmer (2005), Larmat et al. (2009) and Saenger (2011)). The maximum particle velocity is also a suitable imaging condition (Steiner et al., 2008; Lokmer et al., 2009). Alternatively, the divergence and the curl field can be used for imaging conditions that are sensitive to p-waves and s-waves, respectively (Larmat et al., 2009; Lokmer et al., 2009; Horstmann et al., 2015). The strain field has the potential to directly reveal source characteristics (Larmat et al., 2009; Kremers et al., 2011). Additionally, energy densities can be computed from the parameters mentioned above (Artman et al., 2010; Saenger, 2011).

In this study, we focused on the four imaging conditions proposed by Saenger (2011): The maximum particle displacement $\mathbf{I}_d$ was calculated by

$$\mathbf{I}_d(\boldsymbol{x}) = \max_{t \in [0,T]} \|\boldsymbol{u}(\boldsymbol{x},t)\|, \tag{2}$$

with $\boldsymbol{u}(\boldsymbol{x},t)$ being the displacement at each point $\boldsymbol{x}$ in the model at each time t.

The maximum p- and s-wave energy density imaging conditions ($\mathbf{I}_p$ and $\mathbf{I}_s$) were calculated by separating the wavefield in a divergence field and a curl field, followed by the calculation of the energy densities after Dougherty and Stephen (1988):

$$\mathbf{I}_p(\boldsymbol{x}) = \max_{t \in [0,T]} (\lambda + 2\mu)[\nabla \cdot \boldsymbol{u}(\boldsymbol{x},t)]^2, \tag{3}$$

$$\mathbf{I}_s(\boldsymbol{x}) = \max_{t \in [0,T]} \mu[\nabla \times \boldsymbol{u}(\boldsymbol{x},t)]^2. \tag{4}$$

λ and μ represent the Lamé parameters. The maximum total energy density imaging condition $\mathbf{I}_e$ was based on the multiplication of stresses and strains at every point in the model domain:

$$\mathbf{I}_e(\boldsymbol{x}) = \max_{t \in [0,T]} \sum_i \sum_j [\sigma_{ij}(\boldsymbol{x},t)\varepsilon_{ij}(\boldsymbol{x},t)]. \tag{5}$$

$\sigma_{ij}(\boldsymbol{x},t)$ are the stresses and $\varepsilon_{ij}(\boldsymbol{x},t)$ the strains at each point $\boldsymbol{x}$ in the model domain at each time t.

Each of these four imaging conditions was calculated with a different characteristics of the wavefield. Therefore, they enable the independent inspection of the focus point.

2.3 Evaluation of location success

In this study, we want to find prerequisites for the application of TRI. Therefore, it is necessary to be able to evaluate the reliability of the focusing. TRI claims to work with no a priori information about the number of events and their positions in time and space, which implies that results from this method should enable the localization of events unambiguously. The origin time was known for all simulations and we used only one source per simulation. Therefore, the focus was on the location accuracy.

The location of an event can be found by looking for the point with the maximum value in each imaging condition. Because the wavefield was inserted only at discrete points at the surface during the backpropagation, the wavefront needs to heal before being able to focus on the source location. The depth in which the wavefront is healed depends on the discretization of the emitted wavefield (Witten and Artman, 2011). These artefacts were close to the surface and had higher amplitudes than the localization. We observed that on average at a depth of one p-wave wavelength sampling artefacts stopped interfering with the localization of events. Therefore all values above the depth of one p-wave wavelength were set to zero. With the used frequency range and velocity models, this boundary depth was $2.3\,\mathrm{km}$ beneath the free surface. However, muting the upper $2.3\,\mathrm{km}$ of the model inhibits localization of shallow sources. Depending on the expected source depths, this should be considered. In our example application in Southern California, local earthquakes are reported not shallower than $10\,\mathrm{km}$ while the non-volcanic tremor is expected at even greater depths (Horstmann et al., 2015). Therefore, muting the shallow part of the model does not interfere with the event locations in this case.

To evaluate if a certain station distribution enhances reliable locations, a two-step approach was performed: First the location accuracy was determined and locations were sorted as being close to the source or far away. In the second step the intensity of artificial focusing spots was evaluated by introducing four categories. It is crucial to evaluate the intensity of artificial focusing produced with certain setups because they can obscure source locations. In the following, these two steps are described in more detail.

To determine if the location accuracy was adequate, a maximum average deviation threshold was introduced. Locations deviating further away than this threshold were considered to be not successful. The average deviation was calculated as the mean of the error of the source location in all three directions. Therefore, locations could have an error in one direction of up to three times the defined maximum average deviation if the other two directions had exactly the value of the original source location. Consequently, the allowed source area is a octahedron centered at the source location. The maximum average deviation threshold was empirically found to be $1.2\,\mathrm{km}$. The maximum values found in the imaging conditions were either inside the octahedron formed by this threshold or far away from it. To allow this rather large error in locations enabled the focus of this study to be on finding optimal station distributions rather than focusing on very accurate source locations. Finding an appropriate setup to achieve the most accurate source locations possible depends highly on the specific application and is therefore not the focus of this study.

As a second step, each imaging condition that was labelled successful in the first step was normalised by itself and then visualized. Normalising the imaging conditions allowed the direct comparison of different station distributions as well as different imaging conditions. When visualizing the normalised imaging conditions, it proved to be useful to create separate plots containing all points with a certain fraction of the maximum value. Plots were created for values in incremental steps of 0.1, corresponding to a tenth of the maximum value. By viewing all points of the imaging conditions with a specific fraction of the maximum value, successful locations could be assessed further. An example of this plot type is shown in Fig. 1. The top two plots show imaging conditions for the total energy density imaging condition $\mathbf{I}_e$ for two different values (0.6 and 0.9). The middle two plots show the same for the p-wave energy density imaging condition $\mathbf{I}_p$ and the bottom two plots for the maximum displacement imaging condition $\mathbf{I}_d$.

Figure 2 is a one-dimensional representation outlining relevant aspects of the four categories. This representation is equivalent to viewing a one-dimensional profile through the location and noting the values of the imaging conditions along this profile. A peak in Fig. 2 refers to a visible focus in the image and the height of the peak represents the value at the focusing point. The top dashed line in Fig. 2 shows amplitudes of 0.9. This corresponds to the right plots in Fig. 1. All visible spots in the right plots in Fig. 1 translate to peaks higher than 0.9 in Fig. 2. Similarly, the bottom dashed line represents values of 0.6 or $60\,\%$ (left plots in Fig. 1). Depending on the maximum value of peaks outside the designated source area, each imaging condition was sorted into one of four categories:

Category I included the most reliable locations. There was one peak inside the source area corresponding to the location of the event. All other peaks were below 0.6. The plots showing $\mathbf{I}_e$ in Fig. 1 would be categorised into category I.

Category II was similar to Category I but one (or more) secondary peaks were between 0.6 and 0.9. Simulations sorted into this category were considered reliable as well. The plots showing $\mathbf{I}_p$ in Fig. 1 would be sorted into category II because at 0.6 there are multiple black spots and at 0.9 there was only one focus visible.

Category III is depicted in Fig. 2 with two peaks above 0.9. Both of these peaks are inside the source area. In the cases we associated with category III, there was more than one peak but all peaks above 0.6 were within the source area. Therefore, we assumed they belong to the same location. Depending on the type of application, station distributions producing category III locations should be considered carefully.

Category IV simulations were regarded unsuccessful as well although the highest value was found to deviate less than the threshold value from the source. Focusing spots outside of the source area had a peak value of more than 0.9. The plots for $\mathbf{I}_d$ in Fig. 1 would be sorted into this category. In Category IV simulation setups, locations could not be distinguished from artificial focusing spots without knowing the initial source location.

Finally, to determine which simulation setups will produce reliable locations, the simulations with locations in category I and II should be viewed. Simulations with more than one imaging condition in category I or II were considered simulations producing reliable locations. This requirement to have two successful imaging conditions per simulation inhibits the misinterpretation of an artefact for a location. This criterion could be crucial when using real data.

3   The influence of the station distribution

To discover prerequisites for locating seismic sources with TRI, simulations were performed with varying station distributions. Whether the specific setup enhances the localization can be derived from the reliability of locations achieved with that setup.

The reliability of locations is influenced by the amount and position of stations at the surface. The wavefield is only sampled at these discrete positions. Therefore, different aspects of the station distribution were tested systematically to determine which station placements enable a reliable and unambiguous localization.

In the first set of simulations, optimal apertures and inter-station distances were sought for that still produce reliable locations. The ability to locate sources with an array not centred above the source was tested in a second set of simulations. In the third set of simulations, the ability of TRI to cope with heterogeneous station distributions was tested.

These three sets of simulations were performed with nine receivers at the top of the model. Additionally, the effect of using an increased number of receivers was investigated for individual setups. All simulations in this section were performed using a homogeneous velocity model for forward as well as time-reversed simulations. The p-wave velocity was set to $4000\,\mathrm{ms}^{-1}$, the s-wave velocity to $2300\,\mathrm{ms}^{-1}$ and the density to $2000\,\mathrm{kgm}^{-3}$. There was no noise added to the traces. Therefore, the only change between simulations was the station distribution. Presumably, observed differences in location accuracy were caused by the change in the station placement.

3.1 Optimum aperture and inter-station distance

To find the optimal apertures and maximum inter-station distances still enabling the localization with TRI, nine stations were placed in a square and centred above the source location. The distance d between the stations was then increased discretely (see Fig. 3). By increasing the inter-station distance, the aperture of the array is increased as well. When using nine stations in a square layout, the aperture is twice the distance d between receivers. The expected result would be a range of receiver distances producing reliable source locations. The lower bound of this range corresponds to the minimum aperture and the upper bound to the maximum inter-station distance needed to locate a source of the specific type in the specific depth.

In Fig. 4 performed simulations are marked with a grey bar to distinguish gaps in simulations from simulations that did not locate the source successfully. Only successful locations, deviating less than the threshold from the source location, are marked with a symbol corresponding to the imaging condition and a colour corresponding to the category. In all results in this study, $\mathbf{I}_s$ is excluded for explosion sources because the radiation pattern only produces p-waves and therefore does not allow any localization with $\mathbf{I}_s$. Similarly, $\mathbf{I}_p$ is excluded for strike-slip sources because using a homogeneous model it was not possible to locate strike-slip sources with $\mathbf{I}_p$. Three source depths were tested with an explosion and a strike-slip source. Inter-station distances producing locations in category I or II for at least two imaging conditions were considered reliable. Category III locations may introduce ambiguities.

Inter-station distances and subsequently apertures producing reliable locations can be seen in Fig. 4. We were able to locate a strike-slip source in $5\,\mathrm{km}$ depth with nine receivers placed 1 to $9\,\mathrm{km}$ apart. The explosion source in $5\,\mathrm{km}$ depth was located reliably with an inter-station distance of $6\,\mathrm{km}$. For a $11.9\,\mathrm{km}$ deep source, a reliable localization was possible with inter-station distances of 4 to $19\,\mathrm{km}$ for a strike-slip source and 9 to $15\,\mathrm{km}$ for an explosion source. The strike-slip source in $22\,\mathrm{km}$ depth was located with nine receivers spaced 17 to $25\,\mathrm{km}$ apart and the explosion source with receivers spaced 15 to $25\,\mathrm{km}$ apart. The strike-slip source in $22\,\mathrm{km}$ depth could also be located with inter-station distances of 6 to $12\,\mathrm{km}$. However, at an inter-station distance of $15\,\mathrm{km}$ there was only one imaging condition that led to a reliable localization. Therefore only the larger inter-station distances were considered successful for this source depth.

In general, we found that sources in a certain depth could be located with an inter-station distance roughly the same as the source depth and an aperture of twice the source depth which relates to an aperture angle of $90\,^\circ$ to $100\,^\circ$. Additionally, the range for optimal apertures decreased with increasing source depths for strike slip sources but increased with increasing source depths for explosion sources. Furthermore, strike-slip sources could be located with a wider range of inter-station distances

than explosion sources.

In our setup with a homogeneous velocity model, nine receivers were sufficient to locate explosion and strike-slip sources reliably. In Fig. 5, the localization results for an increased number of receivers are shown. Receivers were added outside of the nine original receivers with the same inter-station distance. Receiver distances stayed constant (at $13\,\mathrm{km}$ for this source in $11.9\,\mathrm{km}$ depth) while the aperture was increased. Additionally, receivers were added inside the original array and consequently the aperture was kept constant at $24\,\mathrm{km}$.

Increasing the number of receivers from 9 to 25 increased the accuracy of the localization. 49 receivers slightly enhanced the results further. Using 169 receivers, spaced $2\,\mathrm{km}$ apart, did not improve the location accuracy anymore. For the strike-slip source the location accuracy even decreased for $\mathbf{I}_e$ to a category III location. These results suggest that a slight improvement in location accuracy can be achieved by using more stations. Nevertheless, nine stations produced reliable locations with a homogeneous velocity model and no noise in the traces. The only simulations of this study where all imaging conditions produced a category I location can be seen in Fig. 5 for the strike-slip source when using 25 or 49 stations. An explosion source could not be located with three category I locations.

In addition to the optimal range of inter-station distances, we found that different imaging conditions were sensitive to different source types. While $\mathbf{I}_d$ and $\mathbf{I}_s$ seemed to be successful for a strike-slip source, $\mathbf{I}_e$ and $\mathbf{I}_p$ were more successful for an explosion source. This can be seen especially well when considering only category I locations in Fig. 4 and 5.

3.2 Arrays not centered above source location

To determine the sensitivity of TRI to an event not centred beneath the array, locations were analysed with an array of nine receivers shifted in one direction. In practice, arrays are rarely centred above an event location. Therefore, it is necessary to know in which area of the model sources can be located. This helps to estimate either where to put stations if events are expected in a specific target area or where locations can be successful when using an already existing array.

In this section, the asymmetry of the array in relation to the source location was investigated. Nine receivers were placed in a square using the inter-station distances that produced reliable locations found in the previous section. In Table 1, the used inter-station distance for each source depth can be seen. These nine receivers were moved in negative x direction in order to increase the shift distance s between the centre receiver and the source location (see Fig. 6). For smaller shift distances some part of the array is still above the source. At one shift s the shift distance is equal to the inter-station distance. At this point one of the side receivers is directly above the source location. For larger shifts the source location is beside the array. In Fig. 7 the shift distance s where the source is no longer beneath the array is marked by a dashed line.

In Fig. 7 the results for different shift distances s are shown. A $0\,\mathrm{km}$ shift represents an array that is centred above the source location. Shallow explosion sources, at $5\,\mathrm{km}$ depth, could not be located with an array not centred above the source while strike-slip sources in $5\,\mathrm{km}$ depth could be located with a shift s of $6\,\mathrm{km}$. Reliable locations were possible for the explosion source in $11.9\,\mathrm{km}$ depth at shifts of 6 and $8\,\mathrm{km}$. The strike-slip source in $11.9\,\mathrm{km}$ depth could be located with shifts of 2, 13 and $19\,\mathrm{km}$. In-between those shift distances it can be either located only with one imaging condition or not at all. The explosion

source in $22\,\mathrm{km}$ could be located with shifts from 8 to $13\,\mathrm{km}$ while the strike-slip source in this depth could be located with shifts of $20\,\mathrm{km}$ and $23\,\mathrm{km}$.

Explosion sources could best be located when the centre of the array was directly above the source or when the source was in-between the receivers. It could not be located reliably if the source location was too close to one of the receivers or beside the array. Strike-slip sources could be located if one of the receivers of the array was above or near the source location but they could not be located if the source location was between two stations. Neither the explosion source nor the strike-slip source could be located when the source location was outside the array. The only exception was the strike-slip source in $11.9\,\mathrm{km}$ depth. It could be located reliably with a shift of $19\,\mathrm{km}$.

To further investigate the different behaviour of the localization of explosion and strike-slip sources, simulations were performed with an increased amount of receivers. 25 receivers were placed in a square of 5 by 5. The inter-station distance was set to $8\,\mathrm{km}$ which is smaller than the inter-station distance used for the nine receivers in Fig. 7. An explosion and a strike-slip source in $11.9\,\mathrm{km}$ depth were tested. The results can be seen in Fig. 8. For both source types almost all tested shifts of the array were able to locate the sources reliably. There is no significant difference between simulations where one of the receivers was above the source location ($s = 8\,\mathrm{km}$ and $s = 16\,\mathrm{km}$) and those where the source location was in-between the receivers ($s = 4\,\mathrm{km}$ and $s = 12\,\mathrm{km}$). From a shift distance of $16\,\mathrm{km}$ onwards, the source was beside the array. Both source types could be located reliably when the source was next to the array up to a shift of $32\,\mathrm{km}$ where the source was $16\,\mathrm{km}$ next to the array. At a shift of $24\,\mathrm{km}$, the explosion source could not be located reliably anymore while at a shift of $28\,\mathrm{km}$ the strike-slip source could not be located reliably anymore. An overall decrease in location accuracy was observed when the source was no longer beneath the array.

Overall, an increased amount of receivers with a smaller inter-station distance ensures the localization of strike-slip and explosion sources beneath the whole array. Additionally, a larger array enables the localization of events outside of the array as well. Conclusively, if the source locations are not known a rather large array should be used.

3.3 Irregular station distributions

To determine the influence of heterogeneous inter-station distances on the localization capabilities of TRI, the azimuthal gap a was used. Seismic stations are rarely placed in a square with every receiver the same distance away from the next. Horstmann et al. (2015) introduced the azimuthal gap as the horizontal angle between two stations viewed from the projection of the source to the surface. With nine receivers placed in a square, the azimuthal gap is $45°$ for each station pair, excluding the centre station. When moving the corner stations closer to the source location in x direction, the angle increases between some of the stations and decrease between other stations (see Fig. 9). In this study, the azimuthal gap refers to the maximum angle between stations. The minimum azimuthal gap can be derived by subtracting the maximum azimuthal gap from $90°$ because the corner stations are moved inward from their corner positions in x direction until they meet the next station. At the end, the array is effectively reduced to five stations with homogeneous azimuthal gaps of $90°$. In this synthetic test the array is still symmetric to the source location. However, for larger and potentially more irregular arrays the azimuthal gap indicates if there is a large

gap in the array where no signal is recorded. Depending on the size of this gap, there may not be enough recorded waveforms from that direction and therefore the source reconstruction may become impossible.

In Fig. 10 the localization results are shown. Because the stations could only be moved on the model grid, the resulting azimuthal gaps are spaced differently for the three source depths. We found that the deeper the source the larger the azimuthal gap could be. For a $22\,\mathrm{km}$ deep source, reliable locations were possible with a maximum azimuthal gap of up to $67°$. A $11.9\,\mathrm{km}$ deep source could be located reliably with an azimuthal gap of up to $58°$. The shallow source, in $5\,\mathrm{km}$ depth, did not seem to allow a heterogeneous station distribution.

4 The effect of a complex velocity model

In addition to the station distribution, a complex velocity model may have a strong influence on the localization capabilities of TRI. In general, a sufficiently correct velocity model is needed to be able to backpropagate the wavefield adequately. But also a sufficiently correct velocity model may include complex velocity structures such as low velocity zones or sharp velocity contrasts. These structures can trap energy and obscure the source location. This is why the imaging conditions were divided by an illumination map as described in section 2. However, pronounced artefacts may remain in the final result.

To investigate the extend of focusing errors due to complex velocity structures, four different velocity models were tested. Differently shaped and positioned low velocity zones were tested as well as a fault. Each velocity model was once tested with the low velocity zone or fault known and once with the low velocity zone or fault not known. The velocities in the low velocity zones were 75% of the values from the homogeneous models ($v_p = 4000\,\mathrm{m/s}$). The layered model used four layers and p-wave velocities ranged from $3000\,\mathrm{km}$ to $6000\,\mathrm{km}$. S-wave velocities were calculated with a constant ratio of $v_s = v_p/\sqrt{3}$.

The forward simulation incorporated the structure while one backward propagation was done with the exact same velocity model as the forward simulation and one was done with a homogeneous or layered velocity model instead. For each velocity model, a strike-slip source and an explosion source was tested in $11.9\,\mathrm{km}$ depth. Two sets of receivers, one with nine receivers and one with 25 receivers, were placed in a square and centred above the source. The receivers were spaced $13\,\mathrm{km}$ apart for both sets.

In Fig. 11 the localization results are shown. The results of the two sets of receivers used are shown in the upper and middle part of the plot. The velocity model used for the forward simulation and one of the time-reversed simulations is shown in the lower part of the plot. For the second time-reversed simulation a homogeneous model or a simple layered model was used.

When there is a known low velocity layer above the source (see Fig. 11, left model), both a strike-slip source and an explosion source could be located reliably. There is no drastic improvement when using more receivers. When the low velocity layer above the source was not known, the localization capabilities decreased and a reliable location was no longer possible.

When the source was inside the low velocity layer (see Fig. 11, second model), the localization was not significantly enhanced by using more receivers as well. When this low velocity zone was not known, the reliable localization of a strike-slip source was still possible but not the localization of an explosion source.

When there was a spherically shaped low velocity zone around the source (see Fig. 11, second model from the right), the localization was enhanced when using 25 receivers. A strike-slip source inside a spherically shaped low velocity zone could be located when the low velocity zone was known but not at all when it was not known while an explosion source could still be located when the low velocity zone was not known.

5　　The last velocity model was a layered model with a fault (see Fig. 11, right model). When the fault was known the strike-slip source could be located with 9 and 25 receivers. When it was not known, when just a layered velocity model was used for the backward propagation, the reliability decreased and the source could not be located anymore. An explosion source could not be located successfully, even with 25 receivers.

　　Taken together these results suggest that an increased number of receivers helps only slightly when the velocity model
10　was more complex. Additionally, the localization of strike-slip sources was influenced less by a complex velocity model than explosion sources. If structures like low velocity zones and faults were known, it did not hinder the localization. However, if they are not known, llocation accuracy decreased.

5   Limits for the signal-to-noise ratio

The previous sections used only synthetic seismograms recorded during forward simulations and then re-emitted into the model
15　time-reversed. Real data, however, does not only consist of the signal corresponding to the event. It also includes a variable amount of noise. In theory, TRI works with noisy data (Gajewski and Tessmer, 2005; Witten and Artman, 2011). In this section, the smallest signal-to-noise ratio (SNR) still enabling source locations was investigated. An explosion source and a strike-slip source in $11.9\,\mathrm{km}$ depth were used. 9 and 25 receivers were spaced $13\,\mathrm{km}$ apart and centred above the source. Five different SNR values were used: 1, 0.75, 0.5, 0.25 and 0.1.

20　　The noisy data was created by constructing a time series with random amplitudes and the same time step and length as the seismograms. Afterwards the noise signal was filtered to exclude numerically unstable frequencies above $5\,\mathrm{Hz}$. The amplitudes of this time series were modified to achieve the desired SNR of this noise signal in relation to the seismograms of all stations. The filtered noise signal was afterwards added to the seismograms of all stations. Figure 12 shows example traces of the seismograms without noise and the seismograms with the respective SNR value for a receiver directly above an explosion
25　source. When the SNR decreases, the event signal becomes less and less distinguishable from the noise.

　　Figure 13 shows the localization results. When using nine receivers there was no reliable location possible for both source types. With a SNR of 1 there was only one location in category II and for SNRs down to 0.5 there were only locations in category III. When using 25 receivers it was possible to locate both source types with a SNR as low as 0.25 in category I but only with one imaging condition. The explosion source could be located in category I with two different imaging conditions
30　with a SNR as low as 0.5. Surprisingly, the total energy density imaging condition $\mathbf{I}_e$ seemed to be the most stable one for locating sources of both source types. In the previous sections, $\mathbf{I}_e$ seemed to be not as suitable for a strike-slip source.

13

Overall, these results suggest that the noise level has a higher impact on location accuracy compared to complex velocity models. It was possible to locate sources even if the noise level was too high to distinguish events in the traces. Nevertheless very low SNR hinder a reliable localization which can only partly be compensated by adding more receivers.

6   Application example for Southern California

In previous sections, station distributions were tested systematically to gain insight into the characteristics of array designs that influence localization results. Additionally, results showed that noisy data influence the localization more than a complex velocity model if the velocity model is accurate enough. In this section, a real case scenario from Southern California is mimicked by simulating synthetic seismograms with a real velocity model as well as real station positions. The advantage of using synthetic data is that the true source location is known and therefore the location accuracy can be seen directly. First, the given stations are evaluated for their ability to locate events with a homogeneous velocity model. We show that subsets of the array may enhance location accuracy and how to design an array in this region. In the second part, we estimate the success rate achievable with different station distributions using the velocity model by Zeng et al. (2016) and noisy data.

6.1   Determine localization possibilities using results from previous sections

Horstmann et al. (2015) locate non-volcanic tremor in Southern California near Cholame and use 39 stations. In this study, we took 38 of the 39 stations (the northernmost station was excluded here) and tried to locate synthetic events. The receiver positions were transformed to the same x-y-grid as in Horstmann et al. (2015) and plotted in Fig. 14(a). Additionally, three source positions are plotted. These source positions will be used in the following to test the possibility to locate events with one of three receiver sets derived from the 38 stations in Southern California and two receiver sets suggested as a optimal arrays following the results of the previous sections. As source type, strike-slip sources were used in this section. Strike-slip sources occur more dominantly in the subsurface than explosion sources. The extension of this model in x and y direction is the same as in previous models as well as in Horstmann et al. (2015).

Figure 14(a) shows that the 38 irregular stations extend farther in y direction than in x direction. Because the receivers are so heterogeneously spaced, this set of receivers was not expected to give a reliable localization for any of the three sources. The total amount of stations, however, may counteract the heterogeneous inter-station distances. Additionally, we determined two subsets of receivers with more homogeneous inter-station distances. Two subsets were chosen here: one with 31 stations (see Fig. 14(b)) and one with 20 stations (see Fig.14(c)). For receiver set (b) stations very close to each other were excluded while for set (c) stations were reduced to decrease the total amount of traces, which may impact computation time. Lastly, in Fig. 14(d) and and 14(e) two optimal arrays are suggested, one with 32 stations and one with 20 stations. This array was designed with a homogeneous station distance of $8\,\mathrm{km}$. The arrays were positioned to allow locations in roughly the same areas as in Fig. 14(b) and 14(c). For a real application, the array would be moved to locate events in the specific target area. The inter-station distances and apertures for the arrays can be found in Table 2.

14

The target depths for locations was $10\,km$ to $25\,km$ because bigger events occur at depths as shallow as $10\,km$ while the non-volcanic tremor signals seem to occur deeper (Horstmann et al., 2015). For this target depth range, the results of section 3.1 suggested the aperture should be about $20\,km$ or larger to be able to locate deeper events and the receiver distance should not be larger than about $13\,km$ to include shallower events. When comparing these requirements to the values reported in Table 2, the minimum aperture was greater than $20\,km$ for all four receiver sets. Similarly, the average inter-station distance was smaller than $13\,km$ for all four receiver sets. However, the inter-station distances vary greatly, especially for receiver set (a) and (b).

In Fig. 14 two circles mark areas where events are expected to be located with less or more imaging conditions in better categories. These circles were derived from the results from previous sections where we discovered that sources could be located beneath the array when using fewer stations and slightly outside the array when using an increased amount of receivers. Three source positions were chosen to test the hypotheses of where locations were expected.

Simulations were performed with a strike-slip source and a homogeneous velocity model (see top of Fig. 15). The source was placed at all three source positions and in two depths. The five receiver sets presented in Fig. 14 were tested for their capability to locate these sources.

Locations were possible with receiver set (a) although inter-station distances were very heterogeneous. At source position 1, a reliable location was possible in a depth of $11.9\,km$. At a depth of $22\,km$, a reliable location could not be found. At source position 2 and 3 a location at a depth of $22\,km$ was possible.

Receiver set (b) has a slightly enhanced location accuracy compared to set (a). All sources could be located reliably. This highlights that TRI is rather stable and only small alterations to the station distribution allow a localization of events in multiple depths at different positions in the model.

Receiver set (c) consisted of 20 stations and location accuracy was decreased for the sources in $22\,km$ depth. An explanation for the decreased quality for deeper sources could be the reduced aperture of this receiver set. The source in $11.9\,km$ depth could, however, be located reliably and with all three imaging conditions in category I or II. This is in agreement with previous results suggesting a decrease of sensitivity to the station distribution with depth.

Receiver sets (d) and (e) were suggested as optimal arrays based. In comparison to receiver sets (b), receiver set (d) produced a higher location accuracy while receiver set (e) was located slightly worse than the irregular stations of set (c). For this homogeneous case, the suggested array with 32 stations and regular inter-station distances produced the most accurate locations.

After performing this synthetic study with a homogeneous velocity model, we would decide to use receiver set (b) for locating events in this region if these are the only available stations. If planning to deploy stations, receiver set (d) should be used.

6.2 Synthetic tests to estimate success rate with real data

After finding a suitable receiver set enabling the localization with a homogeneous velocity model in different source depths and at different source positions, the success rate with the real velocity model and noisy data has to be investigated. Therefore, additional simulations were performed.

Zeng et al. (2016) obtain the most current and accurate velocity model for the region in Southern California in which Horstmann et al. (2015) locate non-volcanic tremor. The velocity model is three-dimensional and incorporates p- and s-wave velocities. It was interpolated to fit the used finite difference grid and the density was calculated from the p-wave velocity with the empirical equation by Brocher (2005):

$$
\rho = 1.6612 v_p - 0.4721 v_p^2 + 0.0671 v_p^3 -
$$
$$
0.0043 v_p^4 + 0.000106 v_p^5. \tag{6}
$$

v_p depicts the p-wave velocity in $\mathrm{km s^{-1}}$ and the resulting density ρ is in $\mathrm{g cm^{-3}}$.

In Fig. 15 at the bottom, localization results for simulations with and without added noise are shown. Without any noise, the strike-slip source at position number 1 could be located reliably in $11.9\,\mathrm{km}$ depth with receiver set (b) and in $22\,\mathrm{km}$ depth with receiver set (a). Receiver set (c) was not able to produce any location with the actual velocity model. The suggested receiver sets (d) and (e) produced more accurate locations in these cases with the real velocity model and no noise as well.

When adding noise with a SNR of 1, reliable localizations were possible in both depths with receiver sets (a) and (b). Receiver set (c) was still unable to locate any of the sources. However, receiver set (d) and (e) were able to locate the sources. Receiver set (d) even produced a location of category I for all three imaging conditions.

Receiver set (b) remained the best choice in this case followed by receiver set (a). Both were able to locate three out of four sources. Both sets located the sources with noise reliably. Nevertheless, the suggested arrays with regular inter-station distances were more successful than the irregular arrays.

We would suggest to use receiver set (b) to locate events in this area and avoid ambiguity, because all locations were in category II and there was no location in category III. The success rate of locations in this case is expected to be high inside the grey circles marked in Fig.14 as long as the noise level is not too high. Location accuracy is expected to decreases with increasing distance from the array. If, however, new stations were to be deployed, we would recommend to place them similar to receiver set (d)

7 Discussion

The objective of this study was to investigate the sensitivity of TRI to station distributions while considering complex velocity models and a low signal-to-noise ratio. This is important for (1) estimating the success rate of TRI with a given array and velocity model, (2) decreasing the time needed to adjust the stations (e.g. by choosing only a subset of receivers) and (3) designing an array for locating events in a designated target area.

The method of TRI is straight-forward and can be implemented into most numerical codes that can propagate elastic waves through a medium. In this study, we further improved the workflow of Saenger (2011) which was modified by Witten and Artman (2011). We suggested to visualize all points with certain fractions of the highest value in imaging conditions and proposed a set of categories to quantify the accuracy of source locations. When using real data, the sorting into categories may

5 be obsolete. If the receiver distribution is sufficiently good and the level of noise low enough, all focusing spots appearing in the imaging conditions should represent source locations.

Additionally, we rated the success of locations by the distance between imaged and true source location. The used threshold deviation was calculated as the average deviation from all three directions. Therefore, successful locations for the shallowest source could be at the surface. Surface locations were, however, excluded. This restricted the range for a successful location for

10 the source in $5\,\mathrm{km}$ depth. Consequently, it looked like a source in $5\,\mathrm{km}$ depth was especially hard to locate. However, sources shallower than $10\,\mathrm{km}$ are rarely observed in the region in Southern California (Horstmann et al., 2015).

All simulations in this study were set up with the same frequency range for the source wavelet, the same grid spacing, and the same time step. For explosion sources this setup was numerically stable in the used range of seismic velocities. However, S-waves and surface waves experienced numerical dispersion which cannot be reconstructed during the backpropagation of the

15 wavefield. The numerical dispersion could not be eliminated without reducing the grid spacing and consequently increasing computation time significantly. Therefore, we kept the chosen values. We observed no effect in the results suggesting that dispersive s-waves interfered with the localization. The surface waves were more dispersive than the s-waves but are not relevant for this method and consequently do not interfere with the localization as well. The dispersive surface waves may be an alternative reason why we needed to exclude focusing at the surface.

20 In the used workflow, we muted the top $2.3\,\mathrm{km}$ in the imaging conditions to remove any focusing at the surface. This does not allow for the localization of shallow sources but increases the success rate for deeper sources. Other studies restricted possible focusing to the region around the source location (e.g. Horstmann et al. (2015)). However, we observerd that the difference between areas where locations were reliable and areas where they were not was not clear but rather a transitional zone. Additionally, depending on the velocity model and the position of the source in relation to velocity structures, waves

25 could be scattered and sources could be located outside of this region as well. In contrast to reducing the area where focusing is allowed, we propose to carefully evaluate focusing spots outside of the array.

7.1 Station distribution for reliable a localization

Numerous simulations were performed to test different station distributions for their ability to locate sources of different source types as well as in different depths. In this section the results with a homogeneous velocity model and without any noise added

30 to the synthetic seismograms is discussed.

In general, we found that the inter-station distance should not be larger than the source is deep to enhance the localization with TRI. As we performed all simulations with the same frequency range for the source wavelet in the forward simulation, we were unable to judge the influence of varying wavelengths on localization results. However, inter-station distances found to produce reliable locations in this study were large than half the dominant wavelength ($1.2\,\mathrm{km}$ in our case), which was reported

17

as an optimal inter-station distance by Lokmer et al. (2009). Additionally, location accuracy changed with the source depth suggesting a sensitivity of the inter-station distances to the source depth. This can be explained by the discrete sampling of the backpropagated wavefield. The wavefront needs to heal before the wavefield can constructively interfere and focus on a source location. Witten and Artman (2011) observed that the wavefront is healed at a depth of 1 to 1.5 times the inter-station distance and consequently sources need to be at least as deep as the inter-station distance to be locatable. This is in agreement with our results.

Additionally, we found that the total aperture of the array should be at least twice the source depth. The requirement for large apertures has also been reported in previous studies (e.g.: Artman et al. (2010)). However, this is the first study to present a quantification for the required aperture size.

Most simulations produced reliable location with a homogeneous velocity model and only nine stations. More stations increased the location accuracy slightly and helped counteract effects of a complex velocity model and high noise. However, a significantly larger number of stations did not produce perfect locations. This is contrary to most studies that report a large number of stations is necessary for TRI (e.g. Kremers et al. (2011)). We conclude that the distribution of stations may be more influential than the total number of stations on the localization, which has been reported by Horstmann et al. (2015) as well.

Furthermore, we found that a smaller amount of stations enhances locations only beneath the array. When reducing the inter-station distance and increasing the amount of stations, events could be located outside the array as well. The reliability of locations, however, decreased when sources were outside of the array. This might be crucial when designing an array because the array should be optimally positioned above the targeted source region.

In this study we used the maximum azimuthal gap between stations as an indicator for the sensitivity of location accuracy with irregular inter-station distances and found that up to a certain rate of irregularity sources could still be located. Additionally, we observed that stations could be more irregularly placed the deeper the source location. Comparing our maximum azimuthal gaps to those reported by Horstmann et al. (2015) we find that their azimuthal gaps are roughly twice what we observed to be the maximum azimuthal gap. In our case with nine stations, an increase in the maximum azimuthal gap between two stations subsequently resulted in a decrease in the minimum azimuthal gap between two other stations. The discrepancy with Horstmann et al. (2015) suggests that the minimum azimuthal gap (how close two stations are together) has a higher influence than the maximum azimuthal gap on the localization results. This is also supported by the improvement in location accuracy when using 31 of the 38 stations in the Southern California example. Stations close together were excluded to form a subset of the 38 stations. Alternatively, some studies (e.g. Larmat et al. (2009) or Montagner et al. (2012)) compensate an irregular station distribution by weighing the stations according to an area assigned to each station to improve location accuracy. However, when the aim is a fast and reliable localization method, the gain in location accuracy has to be balanced with the extra computation time needed for weighing the stations.

We performed all simulations once with an explosion source and once with a strike-slip source and observed different location accuracies for the same station distributions. We conclude that for strike-slip sources the receiver directly above the

source has a greater influence on the localization result and for explosion sources the receivers farther away have a greater influence. Explosion sources are therefore more sensitive to the positioning and number of receivers while strike-slip sources are more sensitive to how close a receiver is to the source location. This could also explain the observation of Steiner et al. (2008) that the most accurate locations can be gained when using sources emitting strong s-waves in a vertical direction, as is the case with some strike-slip sources. It suggests their aperture was not wide enough or their inter-station distance too large for locating sources emitting mainly p-waves. Furthermore, this observation dictates that inter-station distances should be small to not produce gaps in the array where strike-slip source cannot be located.

7.2   Evaluation of success rate with real data

Preliminary synthetic studies are typically used to evaluate the location accuracy with TRI achievable with a certain station distribution. Often the first simulations are performed with a homogeneous velocity model. If these simulation are successful and a station distribution yields reliable results, the real velocity model is used. If that is successful again, the real data is used that contains varying amounts of noise. Therefore we used complex artificial velocity models and artificial noise as well as a real velocity model from Southern California to estimate the influence on the localization.

We showed that the velocity model can be rather complex and still does not interfere with the localization if the prominent velocity structures are known. Additionally, we observed that noisy data can hinder the localization. An increased amount of receivers enhanced the location accuracy with noisy data. However, when adding noise to the traces, the same random noise signal is added to all stations. This could unintentionally result in a structured noise that is not random anymore. Nevertheless, when this noisy signal is inserted into the model it will travel in different directions and will interfere differently with each other, thus creating a noisy wavefield.

Furthermore, in some cases we observed an increase in location accuracy when using noisy data compared to simulations without noise and when using irregular spaced stations compared to regular spaced stations in combination with a homogeneous velocity model. This suggests that the introduction of irregularity into the simulation helps to differentiate the source signal from any other part of the waveform and enhances the focusing. Nevertheless, when mimicking a real data problem, very regular inter-station distances produced the most reliable locations.

One additional aspect that could influence the location accuracy is the influence of an asymmetric array. An asymmetric array that extends further in one direction than in the other may decrease location accuracy. We observed, that it may cause the focus to be split into multiple focusing spots and therefore introducing ambiguity. Furthermore, TRI can be used for different scales as well as different applications. In this study we concentrated on the field scale. However, it would be a valuable addition to this study if a similar study would be performed on different scales to see if the same guidelines stay true on other scales as well. If the same general principles hold true for smaller or larger scales, it would suggest that observed effects are inherent of the method.

In this study, the event time was known and run-times were adjusted accordingly. When using real data, the event time is not known and therefore a strategy has to be developed to find accurate event times as well. Possibly, the station distribution,

the velocity model and the noise also have an influence on the event time. This has to be investigated in future studies. Lastly, we observed that different imaging conditions were sensitive to different source types. This could be further investigated to potentially derive the source type from results already obtained while locating the source.

8   Conclusions

This study aimed at investigating the prerequisites for applying TRI on the field scale. We, therefore, systematically tested different station distributions with a homogeneous velocity model and evaluated the resulting locations for their reliability. We focused, thereby, on deeper sources ($> 5\,\mathrm{km}$) and muted the upper part of the model to eliminate artefacts.

We found that the inter-station distance should be not larger than the source depth and the aperture of the array should be at least twice the source depth. Additionally, sources could be located best when they were underneath the array. When using more stations, locations outside of the array became possible. In general, stations should be spaced regularly but the deeper the source the more heterogeneously the stations could be and still achieve reliable locations.

Additionally to this strong sensitivity of the source location accuracy to the station distribution, we found a strong influence of the velocity model on the localization. However, complex velocity structures, like low velocity zones or faults, do not hinder the localization as long as they are incorporated adequately in the model. A high level of noise could, however, inhibit the source location even if the velocity model was homogeneous. An increased amount of stations seemed to increase location accuracy in the presence of noise.

Furthermore, we observed in some cases an increase in location accuracy with an increase in complexity, like adding noise or more irregular stations or a more complex velocity model. This suggests that additional scattering of waves may help the localization. We therefore advise to perform preliminary synthetic studies not only with homogeneous velocity models and regular stations but also incorporating as many complexities as possible to get an accurate estimation of the achievable source location.

We showed that only a few simulations are necessary when performing a preliminary synthetic study to estimate if the given setup will work for TRI. Additionally, we showed that for designing an array that should be used with TRI the target area should be considered. The depth of expected events then dictates the inter-stations distance and aperture of the array. If considering a range of depths, the inter-station distance should fit the shallowest events and the aperture the deepest events.

References

Anderson, B. E., Griffa, M., Ulrich, T. J., and Johnson, P. A.: Time reversal reconstruction of finite sized sources in elastic media, J. Acoust. Soc. Am., 130, EL219–EL225, https://doi.org/10.1121/1.3635378, http://asa.scitation.org/doi/10.1121/1.3635378, 2011.

Artman, B., Podladtchikov, I., and Witten, B.: Source location using time-reverse imaging, Geophys. Prospect., 58, 861–873, https://doi.org/10.1111/j.1365-2478.2010.00911.x, 2010.

Brocher, T. M.: Empirical relations between elastic wavespeeds and density in the Earth's crust, Bull. Seismol. Soc. Am., 95, 2081–2092, https://doi.org/10.1785/0120050077, 2005.

Clayton, R. W. and Engquist, B.: Absorbing boundary conditions for wave-equation migration, Geophysics, 45, 895–904, https://doi.org/10.1190/1.1441094, http://library.seg.org/doi/10.1190/1.1441094, 1980.

Dougherty, M. E. and Stephen, R. A.: Seismic energy partitioning and scattering in laterally heterogeneous ocean crust, Pure Appl. Geophys. PAGEOPH, 128, 195–229, https://doi.org/10.1007/BF01772597, 1988.

Fink, M., Cassereau, D., Derode, A., Prada, C., Roux, P., Tanter, M., Thomas, J.-L., and Wu, F.: Time-reversed acoustics, Reports Prog. Phys., 281, 91–97, 1999.

Gajewski, D. and Tessmer, E.: Reverse modelling for seismic event characterization, Geophys. J. Int., 163, 276–284, https://doi.org/10.1111/j.1365-246X.2005.02732.x, 2005.

Harker, B. M. and Anderson, B. E.: Optimization of the array mirror for time reversal techniques used in a half-space environment., J. Acoust. Soc. Am., 133, EL351–7, https://doi.org/10.1121/1.4798268, http://www.ncbi.nlm.nih.gov/pubmed/23656093, 2013.

Horstmann, T., Harrington, R. M., and Cochran, E. S.: Using a modified time-reverse imaging technique to locate low-frequency earthquakes on the San Andreas Fault near Cholame, California, Geophys. J. Int., 203, 1207–1226, https://doi.org/10.1093/gji/ggv337, https://academic.oup.com/gji/article-lookup/doi/10.1093/gji/ggv337, 2015.

Kocur, G. K., Saenger, E. H., Grosse, C. U., and Vogel, T.: Time reverse modeling of acoustic emissions in a reinforced concrete beam, Ultrasonics, 65, 96–104, https://doi.org/10.1016/j.ultras.2015.10.014, 2016.

Kremers, S., Fichtner, A., Brietzke, G. B., Igel, H., Larmat, C., Huang, L., and Käser, M.: Exploring the potentials and limitations of the time-reversal imaging of finite seismic sources, Solid Earth, 2, 95–105, https://doi.org/10.5194/se-2-95-2011, 2011.

Larmat, C. S., Montagner, J. P., Fink, M., Capdeville, Y., Tourin, A., and Clévédé, E.: Time-reversal imaging of seismic sources and application to the great Sumatra earthquake, Geophys. Res. Lett., 33, https://doi.org/10.1029/2006GL026336, 2006.

Larmat, C. S., Tromp, J., Liu, Q., and Montagner, J. P.: Time reversal location of glacial earthquakes, J. Geophys. Res. Solid Earth, 113, 1–9, https://doi.org/10.1029/2008JB005607, 2008.

Larmat, C. S., Guyer, R. A., and Johnson, P. A.: Tremor source location using time reversal: Selecting the appropriate imaging field, Geophys. Res. Lett., 36, 2–7, https://doi.org/10.1029/2009GL040099, 2009.

Lokmer, I., O'Brien, G. S., Stich, D., and Bean, C. J.: Time reversal imaging of synthetic volcanic tremor sources, Geophys. Res. Lett., 36, 1–6, https://doi.org/10.1029/2009GL038178, 2009.

Montagner, J. P., Larmat, C., Capdeville, Y., Fink, M., Phung, H., Romanowicz, B., Clévédé, E., and Kawakatsu, H.: Time-reversal method and cross-correlation techniques by normal mode theory: A three-point problem, Geophys. J. Int., 191, 637–652, https://doi.org/10.1111/j.1365-246X.2012.05619.x, 2012.

NCEDC: NCEDC (2014), Northern California Earthquake Data Center. UC Berkeley Seismological Laboratory. Dataset., https://doi.org/10.7932/NCEDC, 2014.

Saenger, E. H.: Time reverse characterization of sources in heterogeneous media, NDT E Int., 44, 751–759, https://doi.org/10.1016/j.ndteint.2011.07.011, 2011.

Saenger, E. H., Gold, N., and Shapiro, S. A.: Modeling the propagation of elastic waves using a modified finite-difference grid, Wave Motion, 31, 77–92, https://doi.org/10.1016/S0165-2125(99)00023-2, 2000.

5   Shearer, P. M.: Introduction to Seismology, Cambridge University Press, New York, 2 edn., 2009.

Steiner, B., Saenger, E. H., and Schmalholz, S. M.: Time reverse modeling of low-frequency microtremors: Application to hydrocarbon reservoir localization, Geophys. Res. Lett., 35, https://doi.org/10.1029/2007GL032097, 2008.

Witten, B. and Artman, B.: Signal-to-noise estimates of time-reverse images, Geophysics, 76, MA1–MA10, https://doi.org/10.1190/1.3543570, http://dx.doi.org/10.1190/1.3543570, 2011.

10   Zeng, X., Thurber, C. H., Shelly, D. R., Harrington, R. M., Cochran, E. S., Bennington, N. L., Peterson, D., Guo, B., and McClement, K.: 3-D P- and S-wave velocity structure and low-frequency earthquake locations in the Parkfield, California region, Geophys. J. Int., 206, 1574–1585, https://doi.org/10.1093/gji/ggw217, 2016.
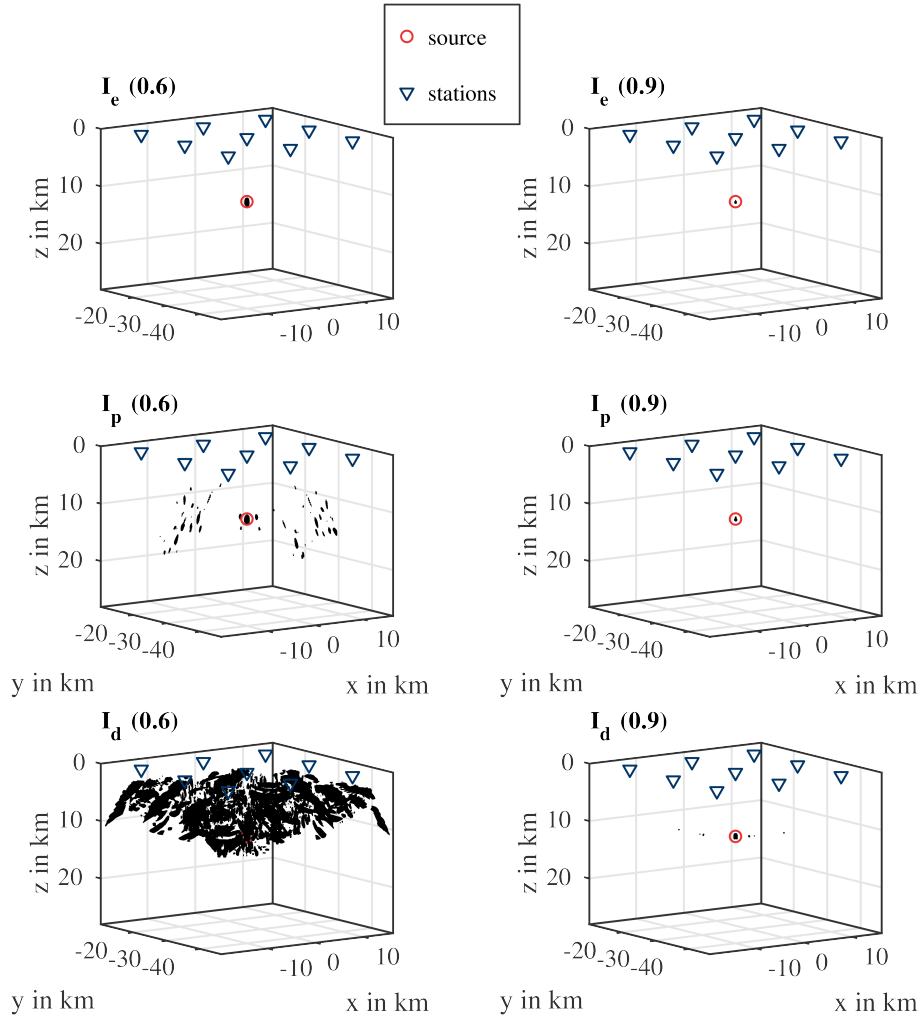
Figure 1. Imaging conditions plotted for one example simulation. Black spots are points having the plotted value (0.6 on the left and 0.9 on the right). $\mathbf{I}_e$ would be classified into category I, $\mathbf{I}_p$ would be classified into category II and $\mathbf{I}_d$ would be classified as category IV and thus be regarded unsuccessful. This example shows an explosion source in $11.9\,\mathrm{km}$ depth with 9 stations placed in a square. The inter-station distance is $13\,\mathrm{km}$. Only the part of the model underneath the stations is shown.
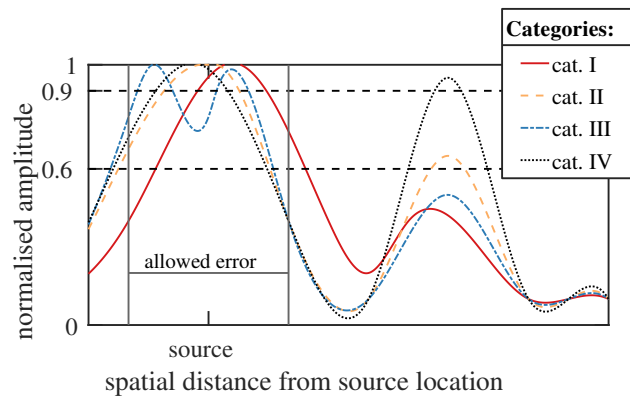
Figure 2. One-dimensional schematic outlining four different categories that were used to rank simulation setups by their location accuracy.
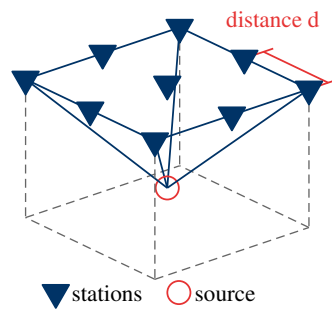
Figure 3. Placement of the nine stations used as receivers for testing the influence of the inter-station distance d. The middle receiver is directly above the source.
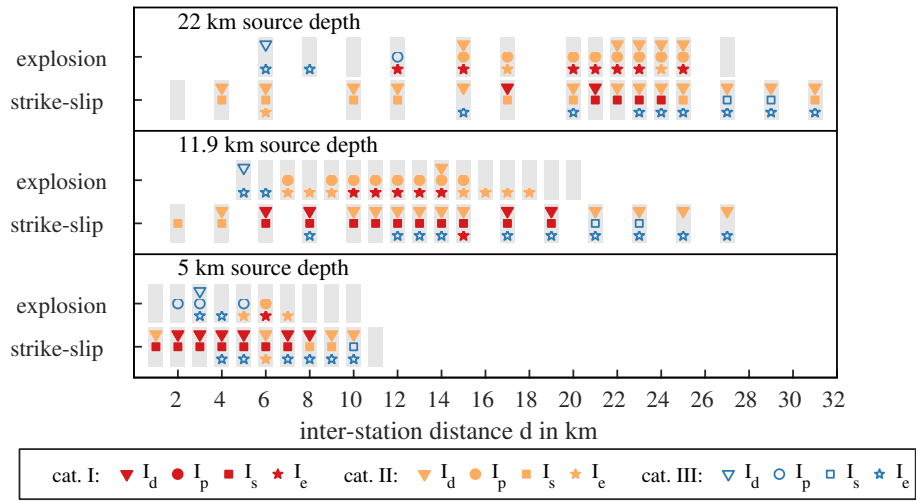
Figure 4. The location accuracy achieved with different inter-station distances d. Three source depths were tested for two source types each. The location accuracies achieved with the individual imaging conditions were ranked according to the categories from Fig. 2. Grey bars indicate setups that were tested. No symbol in the grey bar means the location was not successful. Symbol type and colour in the grey bar represent successful locations with the imaging condition sorted into the respective category.
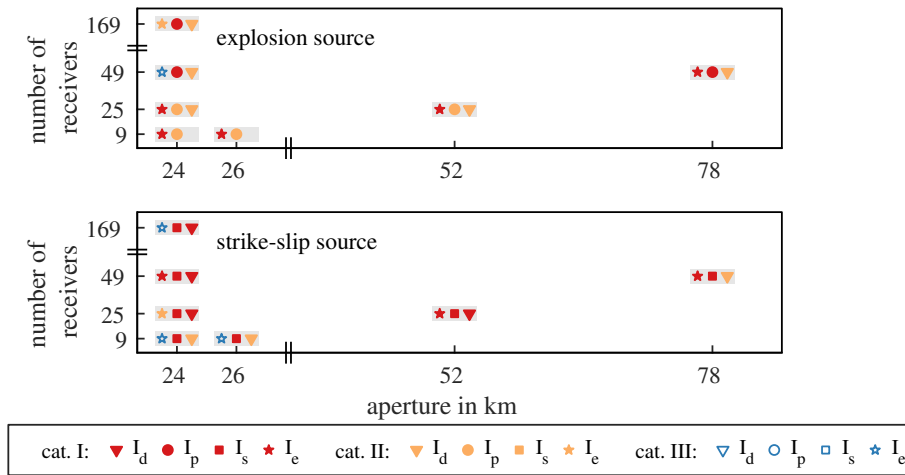
Figure 5. The location accuracy achieved with an increased number of stations. Two source types were tested in $11.9\,km$ depth. Receivers were added either in-between the existing nine stations (aperture stays the same) or outside of the existing nine receivers (aperture increases). The locations achieved with the individual imaging conditions were ranked according to the categories from Fig. 2. Grey bars indicate setups that were tested. No symbol in the grey bar means the location was not successful. Symbol type and colour in the grey bar represent successful locations with the imaging condition sorted into the respective category.

Table 1. Receiver distances used for different source depths according to results from section 3.1

source depth (km)	receiver distance d (km)
5	6
11.9	13
22	23
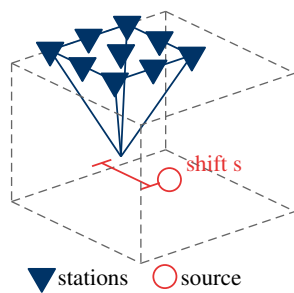
Figure 6. Placement of the nine stations used as receivers for testing the influence of an array that is not centred above the source. The shift s was discretely increased.
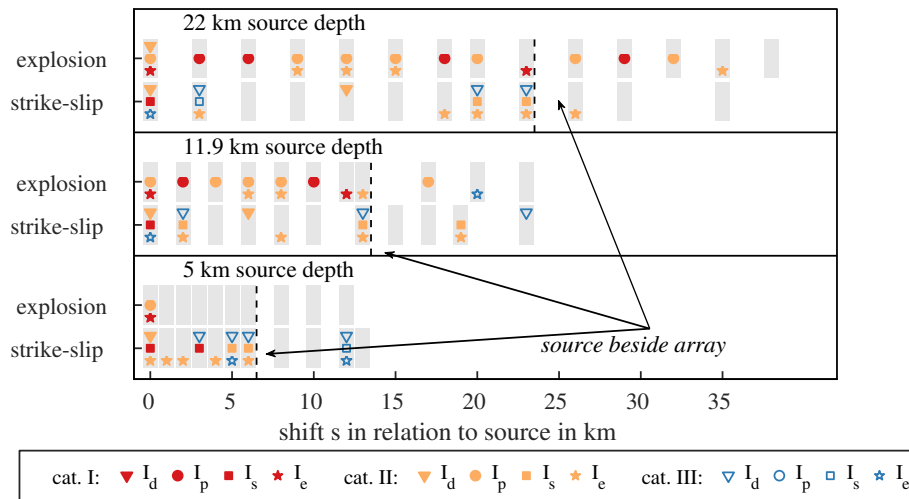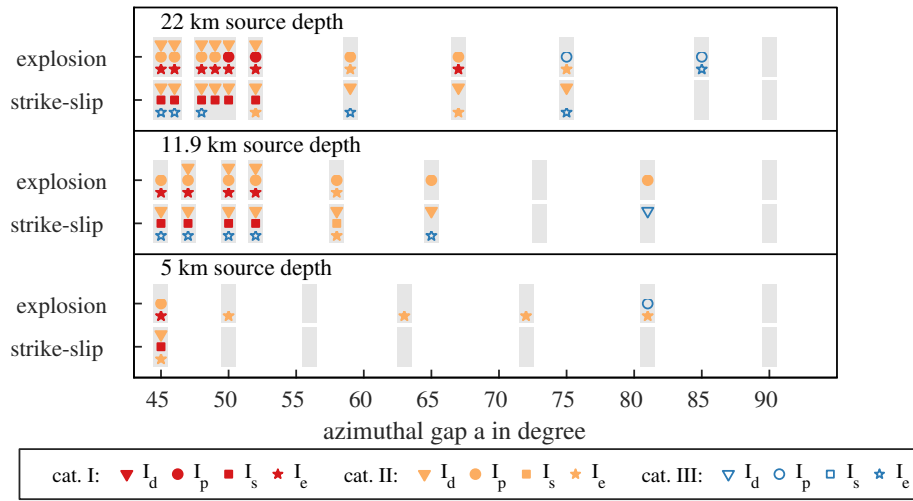
Figure 7. The location accuracy obtained with different shift distances s between the middle of the array and the source location. It is marked at which shifts the array is no longer above the array. Three source depths were tested for two source types each. The locations achieved with the individual imaging conditions were ranked according to the categories from Fig. 2. Grey bars indicate setups that were tested. No symbol in the grey bar means the localization was not successful. Symbol type and colour in the grey bar represent successful locations with the imaging condition sorted into the respective category.
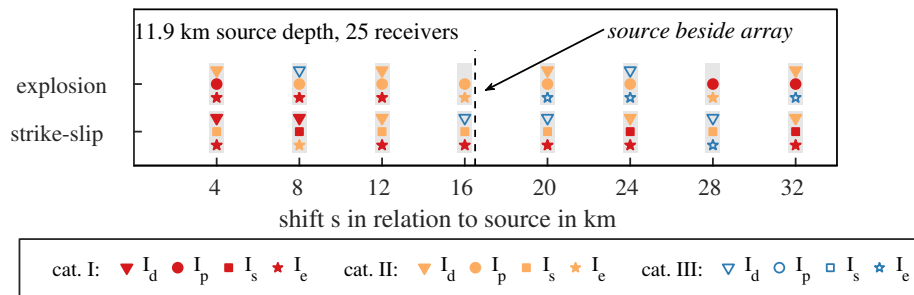
Figure 8. The location accuracy achieved by using 25 instead of 9 stations placed $8\,km$ apart while shifting the array . It is marked at which shifts the array is no longer above the array. A source in $11.9\,km$ depth was tested with two source types. The localization obtained with the individual imaging conditions were ranked according to the categories from Fig. 2. Grey bars indicate setups that were tested. No symbol in the grey bar means the localization was not successful. Symbol type and colour in the grey bar represent successful locations with the imaging condition sorted into the respective category.
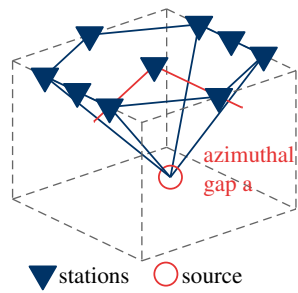
Figure 9. Placement of the nine stations used as receivers for testing the influence of an stations that are distributed heterogeneously. The maximum azimuthal gap a is the largest found angle between two station viewed from the centre station. The azimuthal gap was increased by moving the corner stations closer toward the side receivers on two sides.
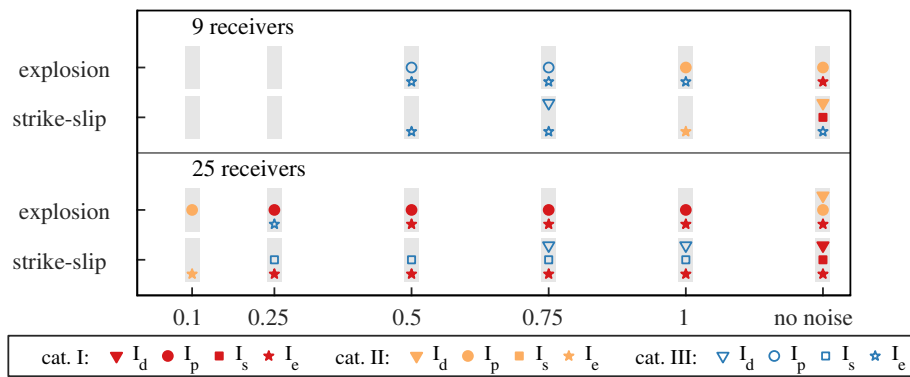
Figure 10. The location accuracy achieved with different maximum azimuthal gaps a. Three source depths were tested for two source types each. The locations obtained with the individual imaging conditions were ranked according to the categories from Fig. 2. Grey bars indicate setups that were tested. No symbol in the grey bar means the localization was not successful. Symbol type and colour in the grey bar represent successful locations with the imaging condition sorted into the respective category.
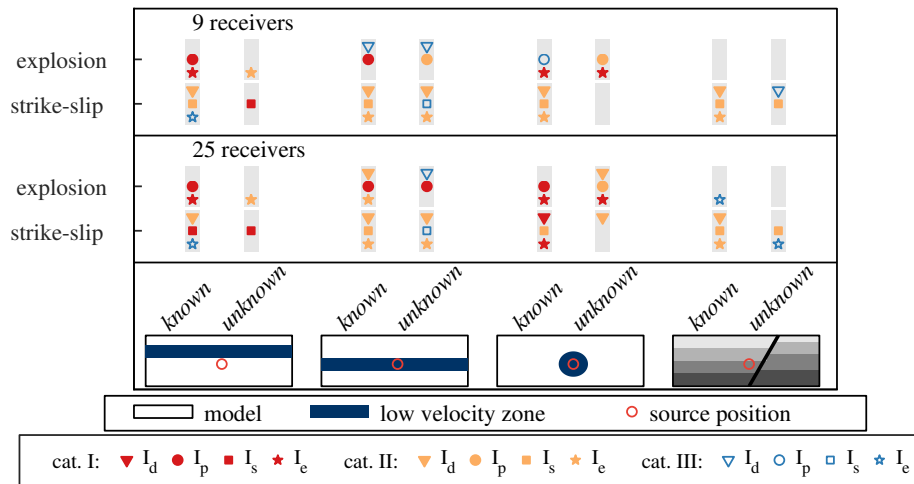
Figure 11. The location accuracy achieved with different velocity models. For each velocity model one simulation was performed with the low velocity zone or fault known and one with a homogeneous or layered velocity model for the backward simulation. A set of nine receivers and a set with 25 receivers was tested. The localization obtained with the individual imaging conditions were ranked according to the categories from Fig. 2. Grey bars indicate setups that were tested. No symbol in the grey bar means the localization was not successful. Symbol type and colour in the grey bar represent successful locations with the imaging condition sorted into the respective category.
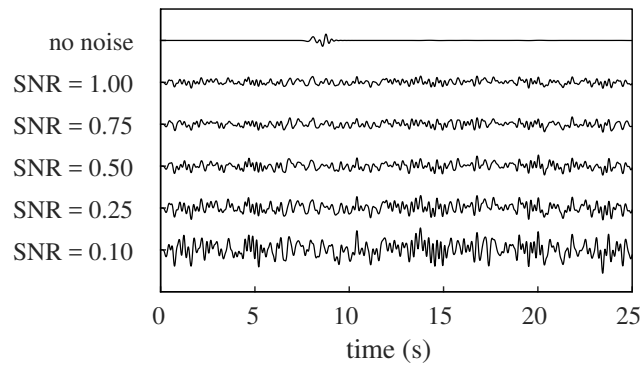
Figure 12. Example traces recorded with a receiver directly above the source for an explosion source placed in $11.9\,km$ depth. The traces without noise and with different degrees of noise are shown, resulting in different signal-to-noise ratios (SNR).
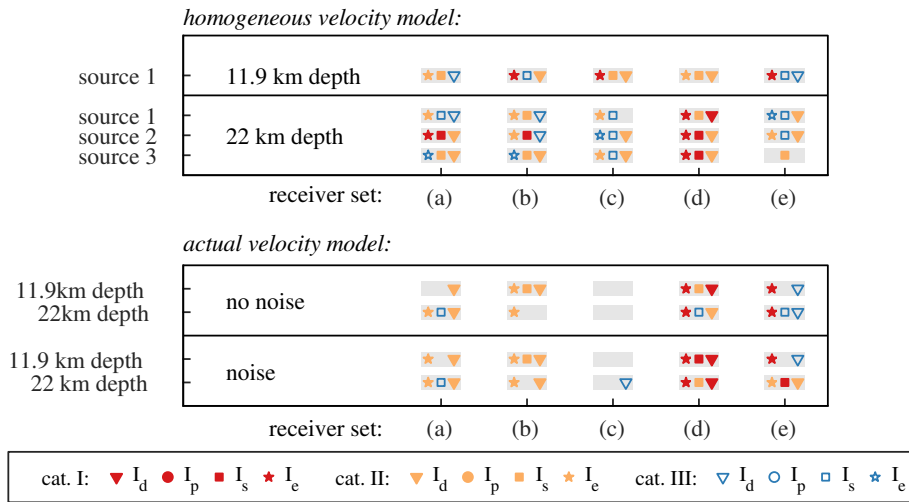
Figure 13. The location accuracy obtained with different amounts of noise added to the traces. A set of nine receivers and a set with 25 receivers was tested for two different source types. The locations obtained with the individual imaging conditions were ranked according to the categories from Fig. 2. Grey bars indicate setups that were tested. No symbol in the grey bar means the localization was not successful. Symbol type and colour in the grey bar represent successful locations with the imaging condition sorted into the respective category.
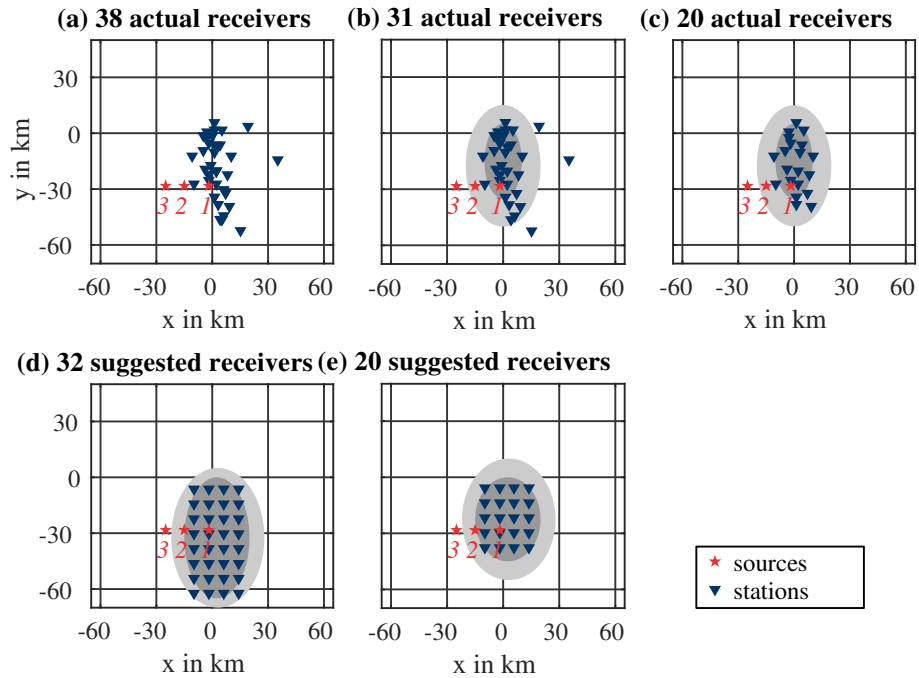
Figure 14. Receiver sets used to test success rate of locations in Southern California: (a) 38 stations as used by Horstmann et al. (2015), (b) a subset of (a) excluding stations that are very close to another station, (c) 20 stations of (a), (d) 32 suggested stations with regular inter-station distances and (e) 20 stations suggested for optimal results. Three source positions are chosen to test the range of localization.

Table 2. Inter-station distances d and apertures a of the five receiver sets shown in Fig. 14

receiver set (from Fig. 14)	number of stations	min d (km)	max d (km)	mean d (km)	min a (km)	max a (km)
(a)	38	0.138	23.94	3.919	45.369	58.487
(b)	31	2.002	23.94	5.224	45.369	58.487
(c)	20	2.901	7.499	5.024	20.348	44.923
(d)	31	8	8	8	24	56
(e)	20	8	8	8	24	32

Figure 15. The location accuracy achieved with a strike-slip source in different depths with the different receiver sets and a homogeneous velocity model (top half) and with the velocity model of Zeng et al. (2016) and added noise (SNR = 1)(bottom half). The lower case letters represent the receivers sets of Fig. 14. The localization obtained with the individual imaging conditions were ranked according to the categories from Fig. 2. Grey bars indicate setups that were tested. No symbol in the grey bar means the localization was not successful. Symbol type and colour in the grey bar represent successful locations with the imaging condition sorted into the respective category.